CO2 convective dissolution in a 3-D granular porous medium: an experimental study

Christophe Brouzet, Yves Méheust, Patrice Meunier

CO_2 convective dissolution in a 3-D granular porous medium : an experimental study

C. BROUZET[a,b], Y. MÉHEUST[c], P. MEUNIER[d]

a. Aix Marseille Univ, CNRS, Centrale Marseille, IRPHE - Marseille, France
b. Université Côte d'Azur, CNRS, Institut de Physique de Nice (INPHYNI), France ; christophe.brouzet@univ-cotedazur.fr
c. Univ. Rennes, CNRS, Géosciences Rennes - UMR 6118, 35000 Rennes, France ; yves.meheust@univ-rennes1.fr
d. Aix Marseille Univ, CNRS, Centrale Marseille, IRPHE - Marseille, France ; patrice.meunier@univ-amu.fr

Résumé :

Le stockage géologique du CO_2 dans les aquifères salins est une mesure prometteuse pour réduire les émissions de ce gaz à effet de serre dans l'atmosphère. Lorsque le CO_2 est injecté dans de telles formations géologiques, il se dissout en partie dans l'eau salée interstitielle, créant ainsi une couche riche en CO_2 et située au dessus de l'eau salée sans CO_2, qui est plus légère. Cela provoque une instabilité convective, qui a surtout été étudiée par des approches numériques et théoriques fondées sur le couplage densitaire entre l'équation de transport du CO_2 dissous et la loi de Darcy. En utilisant à la fois un ajustement d'indice optique et une technique de fluorescence induite par laser, nous avons mesuré expérimentalement les caractéristiques de cette instabilité dans un milieu poreux granulaire 3D surmonté par un réservoir de gaz. Dans la gamme de pression partielle de CO_2 étudiée, les résultats montrent que le taux de croissance de l'instabilité reste constant et se trouve un à trois ordres de grandeur au dessus des prédictions théoriques. Nous démontrons que ces résultats sont compatibles avec un forçage de l'instabilité par des fluctuations de porosité.

Abstract :

Geological storage of CO_2 in deep saline aquifers is a promising measure to mitigate global warming by reducing the concentration of this greenhouse gas in the atmosphere. When CO_2 is injected in the geological formation, it dissolves partially in the interstitial brine, thus rendering it denser than the CO_2-devoid brine below, which creates a convective instability. This instability has been intensively discussed by numerical and theoretical approaches at the Darcy scale, but few experimental studies have characterized them quantitatively. By using both refractive index matching and planar laser induced fluorescence, we measure the onset characteristics of the convective dissolution instability in a 3-D porous medium located below a gas compartment. Within the CO_2 partial pressure range studied, our results highlight that the dimensional growth rate of the instability remains constant and one to three orders of magnitude larger than the predicted value. We demonstrate that these experimental results are consistent with a forcing of convection by porosity fluctuations.

Mots clefs : convective dissolution, Rayleigh-Darcy instability, CO_2 geological storage

1 Introduction

The accumulation of carbon dioxide (CO_2) in the atmosphere due to human activities results in a potentially disastrous global problem. One solution to mitigate this issue is to reduce the anthropogenic emissions to the atmosphere by capturing and storing CO_2 in deep saline aquifers and depleted oil reservoirs [1]. These geological formations, located between 1 and 3 km beneath the Earth's surface, are typically porous and filled with brine. At these depths, the CO_2 becomes supercritical and, once injected, its motion through the reservoir is controlled by fluid mechanics [2]. Being positively buoyant, it first rises to the top of the reservoir, until it encounters an impermeable cap-rock, along which it then spreads horizontally. This leads to the formation of a supercritical CO_2 layer positioned above the brine. By dissolving into the surrounding brine, CO_2 then densifies it locally and creates a negatively buoyant CO_2-enriched brine layer sitting on top of pure brine. Once this new layer is sufficiently thick, it becomes gravitationally unstable, leading to a convective instability with a typical fingering pattern.

The convective instability is classically known to be controlled by the Rayleigh number Ra [2], defined further in the text. Such instability has been extensively studied using a combination of theoretical and numerical approaches with a description of flow based on Darcy's law [3, 4, 5, 6, 7, 8, 9]. These studies focus principally on the onset time of the instability and its main characteristics, such as growth rate or wavelength, but also on the CO_2 dissolution rate. These works have been complemented by experimental studies, which, however, remain more limited [4]. Indeed, a large part of them have been performed in a Hele-Shaw cell, mimicking Darcy's law in an experimental setup without grains or porous structure [10, 11, 12, 13, 14, 15]. The first experiments in Hele-Shaw cell have mainly remained qualitative [10, 13], and the validation of the theoretical predictions for the instability characteristics [15] or for the convective dissolution process scenario [12] have only been reported recently.

The validation of the characteristics of the instability and quantitative characterization of the convective dissolution process, obtained in the theoretical and numerical approaches, therefore remains to be performed in an experiment involving a flow cell containing a porous/granular structure. The presence of the grains may render the convective dissolution process significantly more complex by introducing several ingredients, not considered when assuming Darcy's law in an isotropic and homogeneous continuous medium. First, as a natural porous medium is intrinsically random, it may contain heterogeneities, i.e. variations in porosity and permeability. These heterogeneities may impact the velocity field and thus the concentrations, a phenomenon which may continuously force perturbations [4, 16]. Secondly, the heterogeneity of the solute-advecting pore scale flow and its interaction with molecular diffusion below the Darcy scale are known to induce hydrodynamic dispersion of the solute at the Darcy scale [17]. This process enhances mixing and can be expected to lead to coarsening of the fingering pattern [18] and delay the onset time of instability [19]. Theoretical, numerical, and experimental works have started to study the additional effects of heterogeneities [5, 9, 20], porosity fluctuations [16] and hydrodynamic dispersion [4, 18, 19, 21] on the convective dissolution process. However, the question of whether the description of the instability based on Darcy's law is relevant when pore scale heterogeneities and hydrodynamic dispersion are present remains open.

Here, we study the onset of convective dissolution in a granular porous medium quantitatively, and compare the measurements with predictions of the instability characteristics [5, 6, 7, 8]. We first present the experimental setup that allows us to measure the characteristics of the instability within the medium, before discussing the results obtained on the instability growth rate. Additional results on the wavelength of the instability and on the CO_2 flux are reported in a full length article published recently [22].

2 Materials and methods

2.1 Experimental setup

The experimental setup consists of a 300 mm large, 300 mm high, 7 or 15 mm thick, closed and transparent tank as shown in Fig. 1. Note that the tank thickness e is much smaller than its dimensions in the other directions. In addition, as shown further in the text, the thickness is also much smaller than the typical wavelength of the instability but remains larger than the typical grain sizes used in the experiments. This ensures that the instability remains two-dimensional and allows us to visualise it using a refractive index matching method by looking through a relatively thin but still 3-D porous medium. As in several studies reported in the literature [10, 13, 14, 15], we have chosen to use gaseous CO_2 and water as a pair of immiscible fluids to model the instability in the experimental setup. Note that the physics of the process is completely similar to what it would be if supercritical CO_2 were used (instead of gaseous CO_2), but without the necessity to reach very high pressures experimentally. This experimental system is therefore different from analog fluid experiments performed with miscible fluids, such as MEG (methanol and ethylene glycol) and water [**?**] or PG (propylene glycol) and water [11, 20]. The bottom half of the tank is therefore filled with a porous medium and salt water while the top half contains air at atmospheric pressure and a CO_2 sensor. The salt dissolved in the water is here employed to match the refractive index of the grains. The z-direction points downward and its origin $z = 0$ is set at the interface between the brine within the porous medium and the gas. At time $t = 0$, part of the air in the top half of the tank is removed and replaced by CO_2, leading to a sudden increase of the fraction X_{CO_2} of CO_2 above the porous medium. In this configuration, CO_2 dissolves into the brine in the vicinity of the gas-liquid interface, leading to a density difference $\Delta\rho$ between CO_2-rich brine and pure brine proportional

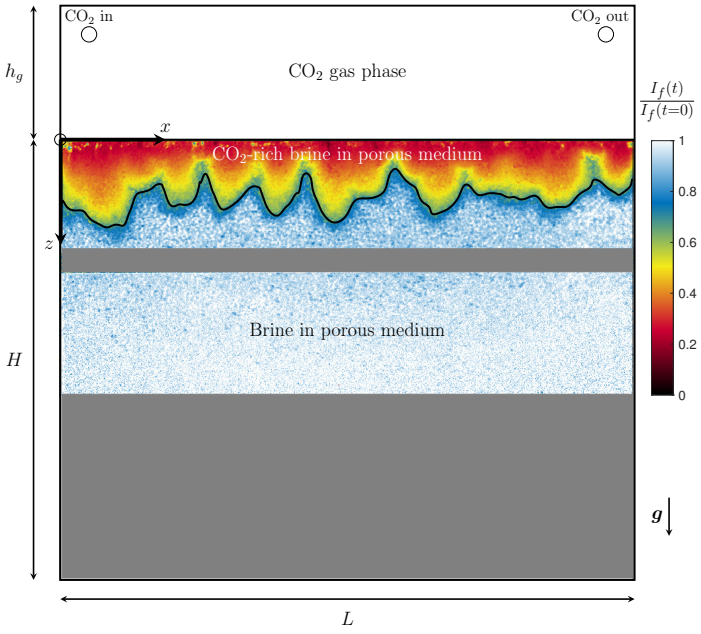

FIGURE 1 – (a) Sketch of the experimental setup. The porous medium, filled with brine, has a height H and the gas phase an height h_g. The thickness of the tank is $e = 15$ or 7 mm, its length is $L = 300$ mm, with a total height $H + h_g = 300$ mm. The gray parts in the image correspond to non accessible zones with the camera : the thin rectangle represents a lateral reinforcement of the tank while the bottom of the tank is not considered as we mainly focus on the onset of the instability.

to the CO_2 partial pressure $P_{CO_2} = X_{CO_2} P_0$ with $P_0 = 1$ bar (see Section 2.4).

In order to visualise the instability inside the porous medium, we use the combination of two different techniques : refractive index matching to see through the porous medium and planar laser induced fluorescence to qualitatively detect CO_2 iso-concentrations. These techniques are presented in the following.

2.2 Porous medium and refractive index matching

Refractive index matching allows for optical access to the bulk of dense suspensions and porous media, by matching the optical indices of the fluid and solid phases and thus canceling any light refraction at solid-liquid interfaces within the flow cell. For the refractive indices of these two phases to be identical, they have to be chosen carefully. Most of the previous works have used highly viscous fluids [17], with a dynamic viscosity μ several orders of magnitude higher than that of water. In order to reach high Rayleigh numbers in our experiments (see Section 2.4) and to stay rather simple with respect to the CO_2 dissolution chemistry, we use FEP (fluorinated ethylene propylene) transparent particles, with a refractive index $n = 1.344$ close to water so that it can be matched with salt water. The FEP particles look like droplets solidified while resting on a surface, as seen in Fig. 2(a). Indeed, they all have a flat side (located at the bottom of the grains in the top inset in Fig. 2(a)) and, at the opposite, a more rounded side. The height of the grains, defined as the distance between these two sides, is on average equal to 1.43 mm. Viewed from the top, they exhibit a clear circular cross section, with a mean diameter of 3.08 mm. The distributions of diameter and height are represented in Fig. 2(a) and show that their dimensions are relatively uniform over the particle population, despite a non-classical shape whose only symmetry is cylindrical. With such grain dimensions, the tank contains therefore between 100 and 200 grains in its width, $50 - 100$ grains in its height, and 5 to 10 particles in its thickness. This is sufficient to consider the assembly of grains as a three-dimensional (3-D) porous medium. Moreover, as the thickness of the tank is about 5 to 10 particles, the flow is fully 3-D in the bulk of the porous medium. The packing of FEP particles has a porosity $\phi = 0.39 \pm 0.02$ and a permeability $K = (9.3 \pm 0.8) \times 10^{-10}$ m^2.

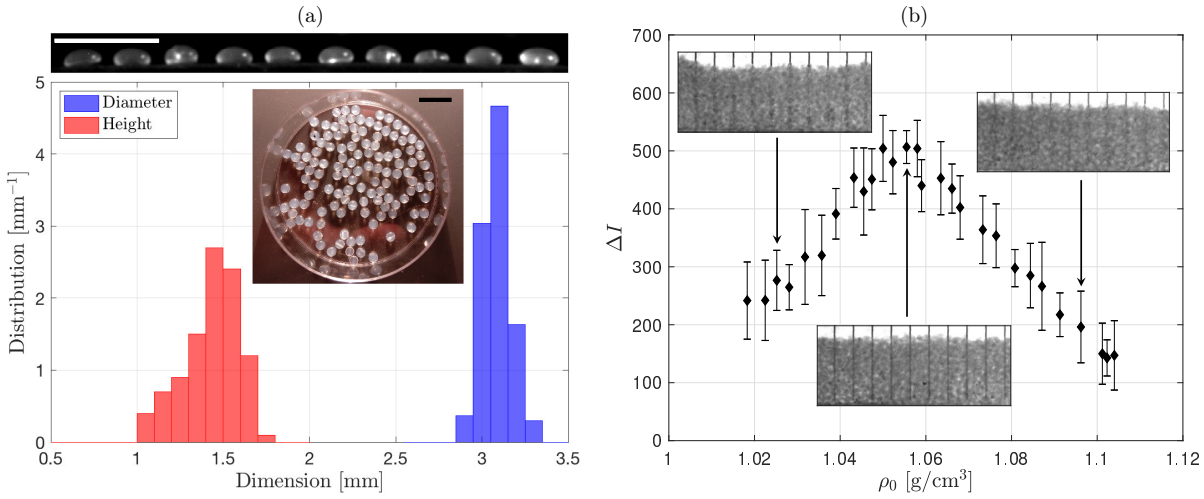

FIGURE 2 – (a) Histograms of grain typical dimensions. The two insets show a side-view (top) and a top-view (middle). The scale bars both indicate 10 mm. (b) Contrast ΔI as a function of the salt water density ρ_0. The three insets show examples of images at different water densities obtained using a white backlight. The spacing between the lines is 10 mm and the error bars are computed from the standard deviation of the set of ΔI measurements obtained for the different lines in the background.

Refractive index matching is performed by adding NaCl salt to the water, in order to reach the FEP's refractive index and make the porous medium as transparent as possible. Note that the presence of salt in the water has a stabilizing influence on the instability [23]. However, adding salt is necessary to match the refractive index, and the concentrations considered remain limited to 1.5 mol/l. In addition, the added salt has been chosen as pure as possible, to limit the presence of other chemical species in the water that may affect the global pH when CO_2 dissolves. The optimal salt concentration, or salt water density ρ_0, has been found by examining the contrast on a pattern composed of vertical dark lines placed behind the tank and under a back-light exposure. The three insets in Fig. 2(b) show typical images obtained in this configuration : on the top, the lines are clearly visible as there are no grains and only salt water. On the bottom, the lines may be distinguished or not, depending on the density of the salt water. The contrast ΔI, defined as the difference between the intensity in the regions without lines in background and the intensity along the lines in the background, is shown as a function of the salt water density in Fig. 2(b). It clearly exhibits an optimal value for the density, in the range $\rho_0 \approx 1.050 - 1.060$ g/cm^3, corresponding to the inset where the lines are the most distinguishable. Note that the porous medium is not completely transparent here, as the grains are not fully transparent and contribute to light attenuation. Such a combination of FEP grains and salt water may therefore not be sufficient for refractive index matching in a 3-D porous medium with large dimensions in all directions, but remains perfectly adapted to the setup described here, where the tank is much thinner in one direction. In the experiments, the salt water has been prepared with a density equal to $\rho_0 = 1.056 \pm 0.002$ g/cm^3.

2.3 Planar laser induced fluorescence

The presence of dissolved CO_2 is visualised using planar laser induced fluorescence. The interstitial fluid, i.e. salt water, contains fluorescein at a uniform concentration of $C_f = 10^{-5}$ mol/l. The tank is illuminated from the top, using a 500 mW laser with a wavelength $\lambda_e = 473$ nm (Laser Quantum, gem 473). From this laser, a laser sheet is obtained with a Powell lens to ensure a homogeneous intensity within the sheet. The intensity of the laser is set to 220 mW and this quantity is kept stable during all the duration of the experiments by proper cooling of the laser. The tank is filmed from its largest side using a 16-bit color camera (Nikon D200) equipped with a green light filter centered around the fluorescein's emission wavelength, $\lambda_f = 515$ nm. As the development of the instability is relatively slow, the frame rate is set to 1 image per minute, while the experiments typically last several hours.

When CO_2 dissolves in the interstitial fluid, it decreases the pH locally, which decreases the re-emitted intensity $I_f(x, z, t)$, as fluorescein light emission and absorption are pH-dependent [24]. However, the CO_2 concentration is extremely sensitive to the pH and the pH strongly depends on the fluorescence function in the pH region corresponding to the saturated concentrations for the CO_2 partial pressures considered in this study [22]. It is therefore not possible to use this method for a quantitative measurement of the CO_2 concentration within the medium. Nevertheless, this method can be used to detect pH iso-curves [14] and therefore iso-concentration lines of CO_2. Figure 3 presents the temporal evolution of the convective dissolution process for an intermediate Rayleigh number (Ra $= 513$), in the top region of the porous medium ($z = 0 - 60$ mm). The visualisation initially exhibits a thin layer with warm colors at the free surface, corresponding to CO_2-rich brine where the pH is reduced, thus lowering the re-emitted intensity. This layer becomes thicker as time evolves and fingers start to develop (Figs. 3(a), (b) and (c)), grow with time (Figs. 3(d), (e) and (f)) and merge (Figs. 3(f), (g) and (h)). At first glance, these visualisations are very similar to the ones obtained in Hele-Shaw cells without grains [15]. However, the fingers seem to be smoother and broader, as the separation between the fingers is not as clear as in

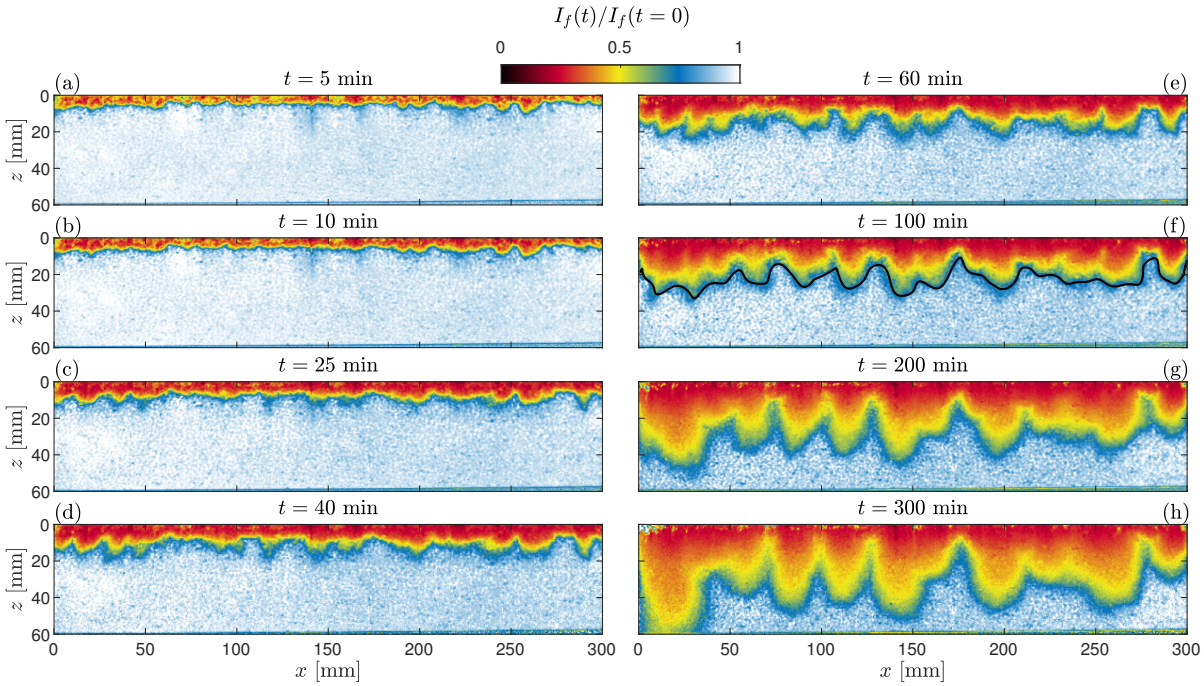

FIGURE 3 – Sequence of images illustrating the instability process. The corresponding times are indicated on top of each image. Panel (f) shows an example of front detection (solid line). The initial partial pressure is $P^0_{CO2} = 0.6$ bar and the thickness of the tank is 7 mm. Note that the bottom of each image does not correspond to the bottom of the tank. A complete video corresponding to this image sequence is available in the supplementary materials of Ref. [22].

Hele-Shaw experiments. This is likely to be due to hydrodynamic dispersion, which enhances the mixing between CO_2-rich brine and pure brine as compared to pure molecular diffusion [18].

Although the relation between the intensity and the CO_2 concentration is not completely quantitative [14], these visualisations can be used to determine the depth of the front at a given intensity. For example the front $z_F(x,t)$ is plotted at a given time t in Fig. 3(f) for an iso-concentration corresponding to $I_f(t)/I_f(0) = 0.65$. At each time t, this front is used to measure the front corrugation amplitude $A(t)$, defined as the standard deviation of the front $z_F(x,t)$ along x [15].

2.4 Governing equations and non-dimensional parameters

The onset of convective dissolution is classically characterised by several scales [3, 4, 8, 12], such as :

$$\mathcal{U} \equiv \frac{K\Delta\rho g}{\mu} \quad \text{for fluid velocities,} \tag{1}$$

$$\mathcal{L} \equiv \frac{\phi D_0}{\mathcal{U}} = \frac{\mu\phi D_0}{K\Delta\rho g} \quad \text{for length scales,} \tag{2}$$

$$\mathcal{T} \equiv \frac{\phi\mathcal{L}}{\mathcal{U}} = \frac{(\mu\phi)^2 D_0}{(K\Delta\rho g)^2} \quad \text{for time scales.} \tag{3}$$

These characteristic scales depend on both the fluid's and porous medium's properties. The velocity scale $\mathcal{U}$ is given by the equilibrium between the gravity force and the viscous term, with K the permeability of the porous medium, g the gravity acceleration, $\mu \approx 1.15 \times 10^{-3}$ Pa.s the dynamic viscosity of the salt water considered in this study and at 20 °C [23]. The density difference caused by the CO_2 dissolution is given by $\Delta\rho = \rho_0 \alpha k_H P^0_{CO2}$, where ρ_0 is the initial density of the salt water, α is the solutal

height	thickness	CO_2 partial pressure	Rayleigh number	Darcy number	other number
H [mm]	e [mm]	$P^0_{CO_2}$ [bar]	Ra	Da $\times 10^7$	$\mathrm{RaDa}^{1/2}$
$138-220$	7 or 15	$0.05-1$	$30-750$	$0.2-0.5$	$0.006-0.12$

TABLE 1 – Different parameters and dimensionless numbers varied in the experiments.

expansion coefficient such as $\alpha k_H = 2.38\times10^{-9}$ Pa^{-1} at 20°C [23], and $P^0_{CO_2}$ is the initial CO_2 partial pressure above the porous medium. The length and time scales $\mathcal{L}$ and $\mathcal{T}$ are obtained by using the velocity scale $\mathcal{U}$, the porosity of the porous medium ϕ, and the diffusion coefficient $D_0 = 1.24\times10^{-9}$ m^2/s in the salt water solution [23].

This convective dissolution problem is characterised by the Rayleigh and Darcy numbers [5, 6, 7, 8, 15]

$$\mathrm{Ra} = \frac{H}{\mathcal{L}} = \frac{\Delta\rho g K H}{\mu\phi D_0}, \tag{4}$$

$$\mathrm{Da} = \frac{K}{H^2}. \tag{5}$$

By varying the different experimental parameters (see Table 1), and mainly the initial CO_2 partial pressure, the Rayleigh number varies from about 30 to 750. It therefore corresponds to unstable configurations since the critical Rayleigh number Ra_c above which the instability starts has been found theoretically to be about 32 [4]. With the parameters given above and in Table 1, the Darcy number belongs to a limited range between $\mathrm{Da} = 0.2\times10^{-7}$ and 0.5×10^{-7}. These values are sufficiently small to prevent any Brinkman effects which were shown to occur when $\mathrm{RaDa}^{1/2}$ becomes of order one [15]. Here, this parameter remains much smaller than 1.

3 Instability growth rate

3.1 Measurements and theoretical predictions

The growth rate of the linear instability is classically measured by plotting the front corrugation amplitude A as a function of time in a log-lin plot [3, 15], as in Fig. 4(a). The growth rate is then determined by fitting the curve with a line, as shown in Fig. 4(a). By performing this fitting operation on all the experiments performed, we can therefore extract the growth rate σ. The fitting time range (approximately [10-40] min) corresponds to the interval where the front amplitude has started to grow while the fingers are not clearly formed (see Figs. 3(b), (c) and (d)) [12, 15]. Fig. 4(b) shows the plot of the growth rate as a function of the initial CO_2 partial pressure, the experimental parameter that can be the most easily varied, for the two tank thicknesses considered here. First, the results are independent of the tank thickness. This tends to indicate that the flow at the Darcy scale is 2-D (i.e. independent of y). However, more surprisingly, the growth rate seems to also be independent of the initial CO_2 partial pressure. Indeed, it remains close to a mean value equal to $\sigma \approx 0.9\times10^{-3}$ s^{-1}, represented by the dashed dotted line in Fig. 4(b). The error bars have been obtained by varying the intensity threshold for the front detection, thus slightly changing the value obtained by the exponential fit of the front corrugation amplitude A.

Using the characteristic scales in Eqs. (1-3), the governing equations of the problem (i.e. the advection-diffusion equation and Darcys' law) become dimensionless and independent of the Rayleigh and Darcy numbers [3, 4, 8, 12]. Indeed, the Rayleigh number simply imposes the boundary condition at the bottom of the reservoir [8], which has no influence on the onset of the instability as it takes place close to

the surface. As a consequence, the growth rate is independent of the Rayleigh and Darcy number in this formulation and was found to be equal to $\sigma^\star = 3 \times 10^{-3}$ numerically [8], and further confirmed experimentally in a Hele-Shaw cell [15]. Note, however, that this growth rate has been obtained without accounting for hydrodynamic dispersion. Going back to dimensional units, the theoretical prediction of the growth rate is therefore simply given by

$$\sigma = \frac{\sigma^\star}{\mathcal{T}} = 3 \times 10^{-3} \frac{(K \rho_0 \alpha k_H P^0_{CO_2} g)^2}{(\mu \Phi)^2 D_0}. \tag{6}$$

This theoretical prediction is plotted as a solid line in Fig. 4(b). It is clear that the theory underestimates the growth rate by about one to three orders of magnitude, depending on the CO_2 partial pressure. This is actually a consequence of the scaling of the theoretical growth rate as $(P^0_{CO_2})^2$ in Eq. (6) whereas the experimental growth rate does not seem to depend on $P^0_{CO_2}$. This discrepancy clearly indicates that the growth of the front corrugation amplitude in our experiments is due to a different mechanism, that may be related to the pore scale flow heterogeneity induced by the presence of the grains. By looking for a relationship between the measured growth rate and the grains, one can remark that the value of the measured growth rate σ is of the order of D_0/d^2, with $d = 1.5$ mm taken as the mean dimension of the grains.

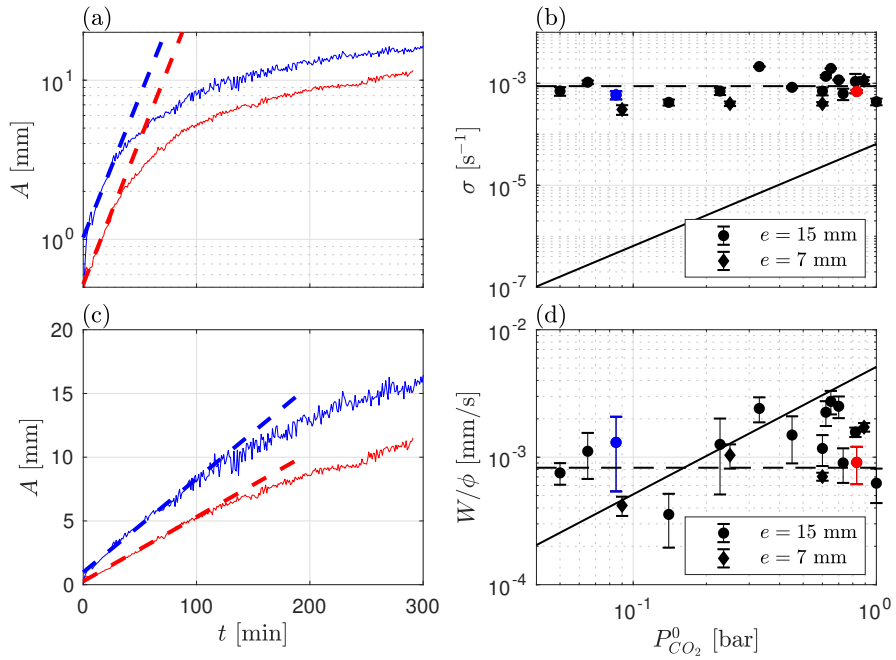

FIGURE 4 – Analysis of the front corrugation amplitude growth. (a) Front corrugation amplitude A as a function of time t in a log-lin scale for two different experiments, at low (blue) and high (red) CO_2 partial pressures. The thick dashed lines correspond to the fits by an exponential function to determine the growth rate. (b) Growth rate σ as a function of initial CO_2 partial pressure in log-log scales. The solid line represents the theoretical prediction [8] while the dashed line shows the trend obtained in the experiments. (c) Front corrugation amplitude A as a function of time t in a lin-lin scale for the same two experiments shown in panel (a). The thick dashed lines correspond to the fits by a linear function to determine the interstitial forcing velocity W/ϕ. (d) Interstitial forcing velocity W/ϕ (see Section 3.2) as a function of initial CO_2 partial pressure in log-log scales. The dashed line represents the trend observed in the experiments, while the solid one corresponds to the typical interstitial velocity $\mathcal{U}/\phi$. The experiments exhibited in panels (a) and (c) are marked with corresponding colors in panels (b) and (d).

3.2 Forcing by porosity fluctuations

To explain our experimental observations, we here propose a model based on a forcing of the instability by porosity fluctuations. Such a mechanism has already been discussed theoretically in a recent paper by Tilton [16]. In this work, he has considered sinusoidal porosity fluctuations and shown that they trigger the instability earlier. Note that this work has been done without considering hydrodynamic dispersion, as it drastically makes the calculation more complex. We have reproduced his calculations using dimensional quantities, considering porosity fluctuations such that

$$\phi = \bar{\phi}[1 + \varepsilon\widetilde{\phi}(x, z)]. \tag{7}$$

Here, $\bar{\phi}$ is the spatially averaged porosity while $\widetilde{\phi}$ stands for porosity fluctuations and ε is assumed to be small. By definition, the porosity fluctuations have a zero spatial average. It is important to note that the porosity variations are considered over length scales larger than the typical grain size d, as the governing equations of the problem are defined by averaging pore-scale continuity, flow and transport equations [16]. Following Tilton [16], we then perform an asymptotic expansion of the governing equations by seeking a solution of the form

$$c(x, z, t) \approx c_b(z, t) + \varepsilon c_1(x, z, t) + ..., \tag{8}$$

with similar expansions for the horizontal and vertical velocities u and w. At zero-order (ε^0), there is no perturbation and the zero-order solution describes the CO_2 diffusion at the top of the porous medium

$$\boldsymbol{v_b} = \mathbf{0} \quad \text{and} \quad c_b(z, t) = 1 - \text{erf}\left(\frac{z}{2\sqrt{D_0 t}}\right) \equiv \frac{2}{\sqrt{\pi}} \int_{z/(2\sqrt{D_0 t})}^{+\infty} \exp(-\tau^2)\mathrm{d}\tau. \tag{9}$$

As a consequence, the order ε^1 represents the typical velocities created by the instability. The advection-diffusion equation becomes [16, 22] :

$$\bar{\phi}\frac{\partial c_1}{\partial t} + w_1\frac{\partial c_b}{\partial z} - \bar{\phi}D_0\boldsymbol{\nabla}^2 c_1 = \bar{\phi}D_0\frac{\partial\widetilde{\phi}}{\partial z}\frac{\partial c_b}{\partial z}. \tag{10}$$

where the right-hand-side of the equation is a forcing term. It therefore appears that the order ε^1 of the asymptotic expansion is forced by the vertical variation of porosity multiplied by the vertical gradient of the diffusion concentration field c_b. This term is expected to trigger the instability due to horizontal variations in the diffusion term of the advection-diffusion equation, brought by local variations in $\widetilde{\phi}$ [16]. Note that this term is strictly null when one does not consider porosity fluctuations, as in classical numerical simulations using Darcy's law with a uniform porosity [3, 8] or Hele-Shaw experiments mimicking experimentally a 2-D porous medium of uniform porosity and permeability [12, 15]. However, in our case, we investigate a 3-D granular porous medium, which is by nature random below the representative elementary volume (REV) characteristic of the Darcy scale [26]. One can therefore expect to have porosity fluctuations that may force some initial velocities. Note however that this implies to some extent that the spatial averaging from pore to Darcy scale is done over a scale that is not quite sufficiently large to be a REV ; in such a way pore scale fluctuations are accounted for in the Darcy scale description as fluctuations in the porosity field, though the porous medium would probably be homogeneous at the Darcy scale if the latter were defined by averaging over a REV.

At the diffusive front, the vertical concentration gradient is initially very large since it scales as $1/\sqrt{D_0 t}$

(as given by the z-derivative of the second equation of (9)). At early stages, the two dominant terms in Eq. (10) are thus $w_1(\partial c_b/\partial z)$ and the forcing term. Equating these two terms leads to the approximation :

$$w_1 \approx \bar{\phi} D_0 \frac{\partial \widetilde{\phi}}{\partial z}. \tag{11}$$

As a consequence, the vertical velocity at order ε^1 is directly forced by the vertical variations of porosity fluctuations. This leads to a forcing velocity of amplitude

$$W = |\varepsilon w_1| = \left| D_0 \frac{\partial \phi}{\partial z} \right|, \tag{12}$$

which is expressed as a Darcy velocity. Following Tilton [16], porosity variations can be decomposed in a sum of porosity perturbations varying sinusoidally in the x-direction. These variations in the horizontal direction trigger the instability by locally making the diffusion of the CO_2-rich brine through the porous medium slightly easier or harder, alternatively. Therefore, despite the fact that $(\partial\phi/\partial z)$ can be of both signs, this term should be considered in Eq. (12) to represent the amplitude of these porosity variations along the horizontal direction, at the scale of the instability.

One can now estimate the evolution of the front corrugation amplitude A. Indeed, the front z_F is advected by the interstitial (i.e. mean pore scale) vertical forcing velocity W/ϕ, such that the front corrugation amplitude A is expected to increase linearly in time in the early stage. This is actually what is observed in the experiments. Indeed, plotting the front corrugation amplitude in linear scale (as done in Fig. 4(c)) indicates that A increases linearly during about 100 minutes. This linear fitting is more efficient than the exponential fitting previously done to extract the growth rate (which seemed to be reasonable only for 40 minutes). The slope of the linear growth of A, i.e. the interstitial forcing velocity W/ϕ, has been measured for all the experiments performed with the FEP grains, and error bars have been obtained by varying the intensity threshold for the front detection. The interstitial forcing velocity W/ϕ is plotted as a function of the initial CO_2 partial pressure in Fig. 4(d), and appears independent of this parameter as shown by the dashed line, with a mean value $W/\phi \approx 10^{-3}$ mm/s. Note that the dispersion of the value found for W/ϕ is larger than the one found for σ. Indeed, the linear fit is more sensitive to the value of the iso-concentration than the exponential fit. However, Fig. 4(d) shows the relative dispersion of data, which remains limited. For comparison, the typical interstitial velocity $\mathcal{U}/\phi$, proportional to $P^0_{CO_2}$, is plotted with a solid line in Fig. 4(d). Both velocities remain on the same order of magnitude, but the scaling with $P^0_{CO_2}$ is clearly different. The experimental results on the forcing velocity W/ϕ are therefore compatible with the value $D_0(\partial\phi/\partial z)/\phi$, which is independent of $P^0_{CO_2}$. Moreover, if one assumes that $(\partial\phi/\partial z) \sim \phi/d$, one can recover quantitatively the mean value of W/ϕ measured in the experiments. This suggests a strong connection between porosity fluctuations and the typical grain size d, as expected since these fluctuations are the Darcy scale signature of pore scale heterogeneity. In the granular porous medium, porosity fluctuations are large at scales close to the typical grain size, and go to zero monotonically as the scale considered for local averaging is increased towards the Darcy scale, which is the scale of the REV. The use of Tilton's model here then implies that the homogenization scale is chosen small enough (i.e. it is somewhat smaller than the REV) for pore scale heterogeneity to translate into spatial fluctuations of the porosity field.

4 Conclusions

In this work, we have demonstrated that the combination of refractive index matching and planar laser induced fluorescence can successfully allow characterizing the onset of the convective dissolution process in a granular, 3-D, porous medium. The experimental results obtained have been compared to predictions mainly obtained using numerical or theoretical approaches assuming Darcy's law in a homogeneous and isotropic porous medium.

The dimensional growth rate σ of the instability has been shown to be constant when the initial CO_2 partial pressure increases by a factor 20. This is in clear discrepancy with the theoretical predictions but can be explained by a model based on porosity fluctuations. Indeed, the experimental results for the growth of the front corrugation amplitude are fully consistent with a forcing of the convection by porosity fluctuations, with a forcing velocity $W = D_0 \partial\phi/\partial z$ found to be on the order of $\phi D_0/d$, i.e. the diffusion coefficient multiplied by the porosity and divided by the typical grain size d in the experiments. As a consequence, the convection is triggered much faster than expected at low CO_2 partial pressures. Indeed, within the time range investigated experimentally (up to $t/\mathcal{T} \approx 300$), only the *diffusive regime* and a small portion of the *linear-growth regime* should be visible [3], while we have observed the development of the instability to much larger extent.

Hence, in order to understand and predict faithfully the onset of this process in sequestration sites, these results show that it is necessary to go beyond the models of flow based on Darcy's law in homogeneous media and to account in some way for the sub-Darcy scale complexity and the heterogeneity of the porous media at all scales.

Acknowledgments

This work was carried out in the framework of the *CO2-3D* Project (ANR-16-CE06-0001) funded by the French National Research Agency (ANR). The authors also acknowledge funding by program "Captage, stockage et valorisation du CO_2" of CNRS MITI. F. Nadal is gratefully acknowledged for fruitful discussions and for providing part of the equipment used in the experimental setup.

Références

[1] B. Metz, O. Davidson, H. de Coninck, M. Loos, L. Meyer, IPCC special report on carbon dioxide capture and storage, Intergovernmental Panel on Climate Change, 2005.

[2] H. E. Huppert & J. A. Neufeld, The fluid mechanics of carbon dioxide sequestration, Annu. Rev. Fluid Mech. 46 (2014) 255.

[3] A. C. Slim, Solutal-convection regimes in a two-dimensional porous medium, J. Fluid Mech., 741 (2014) 461.

[4] H. Emami-Meybodi, H. Hassanzadeh, C. P. Green, J. Ennis-King, Convective dissolution of CO_2 in saline aquifers : Progress in modeling and experiments, Int. J. Greenhouse Gas Control, 40 (2015).

[5] J. Ennis-King, I. Preston, L. Paterson, Onset of convection in anisotropic porous media subject to a rapid change in boundary conditions, Phys. Fluids, 17 (2005) 084107.

[6] A. Riaz, M. Hesse, H. A. Tchelepi, F. M. Orr, Onset of convection in a gravitationally unstable diffusive boundary layer in porous media, J. Fluid Mech., 548 (2006) 87.

[7] H. Hassanzadeh, M. Pooladi-Darvish, D. W. Keith, Scaling behavior of convective mixing, with application to geological storage of CO_2, AIChE J., 53 (2007) 1121.

[8] M. T. Elenius & K. Johannsen, On the time scales of nonlinear instability in miscible displacement porous media flow, Comput. Geosci., 16 (2012) 901.

[9] M. De Paoli, F. Zonta, A. Soldati, Influence of anisotropic permeability on convection in porous media : Implications for geological CO_2 sequestration, Phys. Fluids, 28 (2016) 056601.

[10] T. J. Kneafsey & K. Pruess, Laboratory flow experiments for visualizing carbon dioxide-induced, density-driven brine convection, Transp. Porous Med., 82 (2010) 123.

[11] S. Backhaus, K. Turitsyn, R. E. Ecke, Convective Instability and Mass Transport of Diffusion Layers in a Hele-Shaw Geometry, Phys. Rev. Lett., 106 (2011) 104501.

[12] A. C. Slim, M. M. Bandi, J. C. Miller, L. Mahadevan, Dissolution-driven convection in a Hele–Shaw cell, Phys. Fluids, 25 (2013), 024101.

[13] M. Seyyedi, B. Rostami, R. Nazari Moghaddam, M. Rezai, Experimental study of density-driven convection effects on CO_2 dissolution rate in formation water for geological storage, J. Nat. Gas Sci. Eng., 21 (2014) 600.

[14] C. Thomas, L. Lemaigre, A. Zalts, A. D'Onofrio, A. De Wit, Experimental study of CO_2 convective dissolution : The effect of color indicators, Int. J. Greenhouse Gas Control, 42 (2015) 525.

[15] A. Vreme, F. Nadal, B. Pouligny, P. Jeandet, G. Liger-Belair, P. Meunier, Gravitational instability due to the dissolution of carbon dioxide in a Hele-Shaw cell, Phys. Rev. Fluids, 1 (2016) 064301.

[16] N. Tilton, Onset of transient natural convection in porous media due to porosity perturbations, Journal of Fluid Mechanics, 838 (2018) pp. 129–147.

[17] M. Souzy, H. Lhuissier, Y. Méheust, T. Le Borgne, B. Metzger, Velocity distributions, dispersion and stretching in three-dimensional porous media, J. Fluid Mech., 891 (2020) A16.

[18] L. Wang, Y. Nakanishi, A. Hyodo, T. Suekane, Three-dimensional structure of natural convection in a porous medium : Effect of dispersion on finger structure, Int. J. Greenhouse Gas Control, 53 (2016) 274.

[19] J. Dhar, P. Meunier, F. Nadal, Y. Méheust, Convective Dissolution of Carbon Dioxide in two- and three-dimensional Porous Media : the Impact of Hydrodynamic Dispersion, arXiv : 2110.03803 (2022).

[20] E. Agartan, L. Trevisan, A. Cihan, J. Birkholzer, Q. Zhou, T. H. Illangasekare, Experimental study on effects of geologic heterogeneity in enhancing dissolution trapping of supercritical CO_2, Water Resour. Res., 51 (2015) 1635.

[21] J. J. Hidalgo and J. Carrera, Effect of dispersion on the onset of convection during CO_2 sequestration, J. Fluid Mech., 640 (2009) 441.

[22] C. Brouzet, Y. Méheust, P. Meunier, CO_2 convective dissolution in a three-dimensional granular porous medium : An experimental study, Phys. Rev. Fluids, 7 (2022) 033802.

[23] V. Loodts, L. Rongy, A. De Wit, Impact of pressure, salt concentration, and temperature on the convective dissolution of carbon dioxide in aqueous solutions, Chaos, 24 (2014) 043120.

[24] H. Diehl & R. Markuszewski, The fluorescence of fluorescein as a function of pH, Talanta, 36 (1989) 416.

[25] T. Lacassagne, S. Simoëns, M. El Hajem, J.-Y. Champagne, Ratiometric, single dye, pH sensitive inhibited laser-induced fluorescence for the characterization of mixing and mass transfer, Exp. Fluids, 59 (2018) 21.

[26] G. de Marsilly, Quantitative Hydrogeology : Groundwater Hydrology for Engineers, Academic Press, San Diego, 1986.